Numerical investigation of incompressible flow in grooved channels.
Part 1. Stability and self-sustained oscillations

By N. K. GHADDAR, K. Z. KORCZAK, B. B. MIKIC
AND A. T. PATERA

Department of Mechanical Engineering, Massachusetts Institute of Technology,
Cambridge, MA 02139

Incompressible moderate-Reynolds-number flow in periodically grooved channels is investigated by direct numerical simulation using the spectral element method. For Reynolds numbers less than a critical value R_c the flow is found to approach a stable steady state, comprising an 'outer' channel flow, a shear layer at the groove lip, and a weak re-circulating vortex in the groove proper. The linear stability of this flow is then analysed, and it is found that the least stable modes closely resemble Tollmien–Schlichting channel waves, forced by Kelvin–Helmholtz shear-layer instability at the cavity edge. A theory for frequency prediction based on the Orr–Sommerfeld dispersion relation is presented, and verified by variation of the geometric parameters of the problem. The accuracy of the theory, and the fact that it predicts many qualitative features of low-speed groove experiments, suggests that the frequency-selection process in these flows is largely governed by the outer, more stable flow (here a channel), in contrast to most current theories based solely on shear-layer considerations. The instability of the linear mode for $R > R_c$ is shown to result in self-sustained flow oscillations (at frequencies only slightly shifted from the originating linear modes), which again resemble (finite-amplitude) Tollmien–Schlichting modes driven by an unstable groove vortex sheet. Analysis of the amplitude dependence of the oscillations on degree of criticality reveals the transition to oscillatory flow to be a regular Hopf bifurcation.

1. Introduction

Flow over grooves and in grooved channels arises in a large number of important engineering applications. Examples range from high-speed phenomena such as noise generation and buffeting due to flow over airframe cutouts (e.g. Karachmeti 1956), to low-speed applications such as coolant flow over electronic devices and circuit boards (e.g. Arvizu & Moffatt 1982). In addition to any direct practical import, groove flows serve as a simple, yet rich, example of separated flow, in which the complex interactions of separated vortices, free shear layers, and driving wall-bounded shear flows can be examined in some detail.

The most noticeable feature of experiments on low-speed boundary-layer flows over grooves is the existence of large-amplitude self-sustained oscillations (Reihman 1967; Sarohia 1977). The critical Reynolds number for the onset of unsteadiness, as well as the frequency of the resulting oscillations, is found to be a strong function of the

geometric parameters of the problem. It is clear from the available experimental evidence that these low-speed oscillations are the result of a hydrodynamic instability of the cavity shear layer, and not of an acoustic resonance phenomenon.

Analytical attempts to predict and understand the occurrence and frequency of incompressible groove oscillations have not been overly successful. In particular, vortex-sheet methods, although ostensibly physically appropriate, have proved to be of limited utility owing to indeterminate singularities at separation and re-attachment (e.g. Durbin 1984). Furthermore, most numerical work on incompressible flow over grooves (Pan & Acrivos 1967; Metha & Lavan 1969; Gatski & Grosch 1984), although providing insight into separated flows, has been at too low a Reynolds number to reproduce the experimentally observed self-sustained oscillations. In summary, there is, to date, a very incomplete understanding of hydrodynamic instability and subsequent nonlinear oscillation in incompressible separated flows in groove and related geometries.

It should be noted that groove oscillations are just one example of the much more general phenomenon of self-sustained oscillations in separated flows (for a review see Rockwell & Naudascher 1979). Related by the common feature of shear-layer instability, natural oscillations are found in internal slit flows, groove flows, and channel expansions, as well as external flows involving bluff-body separation. Although it is certainly true that these various manifestations of oscillatory instability are outwardly similar, the extent to which they are amenable to a common underlying theory remains an open question.

In this paper, we investigate by direct numerical simulation the flow of an incompressible fluid in a two-dimensional periodically grooved channel. In §2, the full problem statement is given, and the numerical techniques used briefly described. Stable steady states for the grooved-channel flow are calculated in §3 and the properties of these flows discussed. In §4, the linear stability of the separated flows calculated in §3 is investigated by direct numerical simulation, and a theory proposed for frequency selection based on excitation of stable Tollmien–Schlichting waves. The extent to which this theory applies to other separated-flow instabilities is briefly discussed. Lastly, §5 shows that self-sustained oscillations result from the instability predicted in §4, and the transition to oscillatory flow is demonstrated empirically to correspond to a regular Hopf bifurcation. In Part 2 of this paper (Ghaddar, Magen, Mikic & Patera 1985), we extend our subcritical results to the case of forced flow, and demonstrate that excitation of the flow at its natural frequency results in significant transport enhancement.

2. Problem Formulation and Numerical Methods

2.1. *Governing equations*

The geometry to be considered is the periodically grooved channel shown in figure 1, assumed infinite in extent in the streamwise x and spanwise z directions. The flow is assumed to be fully developed in x, and to be independent of spanwise co-ordinate z. We have chosen the periodic channel configuration (rather than, say, an isolated groove in a boundary layer) not only because of our particular application (compact heat exchangers, cooling of electronic components), but also because periodicity and bounded domains allow minimal ambiguity in terms of boundary-condition specification.
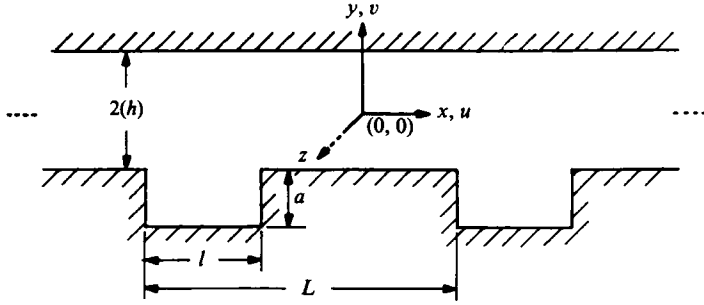
FIGURE 1. The geometry of the periodically grooved channel is described by the groove depth a, the groove length l, and the separation distance between grooves L, all non-dimensionalized with respect to the channel half-width h. All results presented are for flow which is fully developed in x, corresponding to an infinite number of grooves.

To put the problem in non-dimensional form, we scale all velocities by $\frac{3}{2}V$, where V is the cross-channel average velocity,

$$V = (2h)^{-1} \int_{-h}^{h} u(x = 0, y, t) \, \mathrm{d}y,$$

and all lengths by the channel half-width h. (Unless otherwise stated, all variables considered henceforth are assumed to be non-dimensionalized in terms of V and h.) The governing equations for incompressible flow in the domain D can then be written as

$$v_t = v \times \omega - \nabla \Pi + R^{-1} \nabla^2 v \quad \text{in } D, \tag{1a}$$

$$\nabla \cdot v = 0 \quad \text{in } D, \tag{1b}$$

where $v(x, t)$ $(= u\hat{x} + v\hat{y})$ is the velocity, $\Pi = p + \frac{1}{2}v \cdot v$ is the dynamic pressure, $\omega = \nabla \times v$ is the vorticity, and $R = \frac{3}{2}Vh/\nu$ is the Reynolds number, where ν is the kinematic viscosity of the fluid. In addition to R, the flow is governed by the geometric parameters L, l, and a, respectively representing periodicity length, groove length, and groove depth.

The fully developed boundary conditions for the velocity $v(x, t)$ are

$$v(x, t) = 0 \quad \text{on } \partial D, \tag{2a}$$

$$v(x + mL, y, t) = v(x, y, t), \tag{2b}$$

corresponding to no-slip and periodicity respectively. Here ∂D corresponds to the boundary made up of the top and bottom walls of the channel, and m is an integer periodicity index that must be determined empirically (see §§3–5 below). For the pressure we require

$$\Pi(x, t) = -\Pi_x(t) \, x + \Pi'(x, t), \tag{3a}$$

$$\Pi'(x + mL, y, t) = \Pi'(x, y, t), \tag{3b}$$

where the term $\Pi_x(t)$ is the driving force for the flow, and is determined by the imposed flow-rate condition

$$Q = \int_{-1}^{1} u(x = 0, y, t) \, \mathrm{d}y = \frac{4}{3}. \tag{4}$$

Note that the linear pressure term in $(3a)$ is consistent with periodicity of the velocity $(2b)$, as only the gradient of the pressure enters into $(1a)$.

In addition to the full nonlinear problem described by (1)–(4), it is also of interest to consider the linearized problem about a steady solution to the Navier–Stokes equations $v_s(x)$ in which we assume solutions of the form

$$v(x, t) = v_s(x) + \epsilon v'(x, t) \quad (\epsilon \ll 1). \tag{5}$$

Inserting (5) into (1), and neglecting terms $O(\epsilon^2)$ and higher, gives the following linear equation for $v'(x, t)$:

$$v'_t = v_s \times \omega' + v' \times \omega_s - \nabla \Pi' + R^{-1} \nabla^2 v', \tag{6a}$$

$$\nabla \cdot v' = 0. \tag{6b}$$

The boundary conditions on the perturbation v', Π' are as in (2)–(3), but the flow-rate condition (4) is now replaced with

$$Q' = \int_{-1}^{1} u'(x = 0, y, t) \, \mathrm{d}y = 0, \tag{7}$$

corresponding to no net perturbation flow. As for the nonlinear problem, we require initial conditions on the velocity in order to complete the problem specification.

For sufficiently large times, the solution of the initial-value problem (6) will approach the least stable mode of the eigenvalue problem resulting from normal mode formulation of the same equation. In particular, the initial-value-problem result can be interpreted as

$$v'(x, t) \sim \exp(\sigma t) \, \mathrm{Re}\{\hat{v}(x) \exp(2\pi \mathrm{i}\Omega t)\} \quad (t \to \infty), \tag{8}$$

from which the growth rate σ and frequency Ω of the most unstable mode can be inferred. It should be noted that, as implemented here, linear-theory direct simulation isolates only the least-stable mode of the system.

2.2. *Numerical methods*

The numerical approach followed here is that of direct simulation, in which initial-value-problem solvers are used in all aspects of the work. In particular, steady-states, their linear stability, and nonlinear oscillations are all determined using the same basic initial-value code, with only the interpretation of the results depending on the particular physical phenomenon of interest (e.g. (8)). This approach has been used previously for solution of flow problems in simple geometries using spectral methods (Orszag & Patera 1983; Marcus 1984).

We first describe the time-stepping method used, and subsequently discuss the associated spatial discretization. The time-stepping scheme is a primitive-variable fractional step method (Orszag & Patera 1983, Korczak & Patera 1985), in which the Navier–Stokes equations, (1) or $(6a)$, are split into an explicit convective step (third-order Adams–Bashforth), a pressure step to impose incompressibility, $(1b)$ or $(6b)$, and an implicit (Crank–Nicolson) step for the viscous contributions. Numerical implementation of the constant-flow-rate condition, (4) or (7), in the context of the primitive-variable scheme is done by a Green-function technique (Ghaddar, Karniadakis & Patera 1985).

To solve the hyperbolic and elliptic equations generated by the time-stepping scheme described above, we use a spectral element spatial discretization (Patera 1984; Korczak & Patera 1985; Karniadakis, Bullister & Patera 1985), a high-order finite-element method that combines the generality of the finite-element method

(Strang & Fix 1973) with the accuracy of spectral techniques (Gottlieb & Orszag 1977). In the isoparametric spectral element discretization, the domain is first broken down into a series of general quadrangular elements, and the dependent and independent (geometry) variables then represented as high-order elemental Lagrangian interpolants through Chebyshev collocation points. The convective terms in the governing equations are treated by (explicit) collocation, while the (implicit) pressure and diffusive contributions are handled using variational projection operators. Our treatment of elliptic equations is similar to other high-order finite-element techniques, such as the p-type finite-element schemes (Babuska & Dorr 1981), and the global element method (Delves & Hall 1979).

As regards accuracy, it has been shown for numerous problems (Patera 1984; Korczak & Patera 1985) that, for sufficiently smooth solutions, the spectral element discretization shares the exponential convergence rate of global spectral methods. The element decomposition allows for very flexible resolution and point distribution, often yielding solutions more accurate than corresponding global spectral results (Basdevant *et al.* 1985). Furthermore, unlike global spectral methods, the implementation and efficiency of the spectral element method does not rely on simple geometry or specific expansions. For instance, efficiency in the elliptic solvers is achieved by the general procedure of static condensation (Przmieniecki 1963; Korczak & Patera 1985) which, with no restriction on geometry, gives operation counts competitive with corresponding low-order techniques (Patera 1985). In three space dimensions, conjugate gradient iteration is used to solve the implicit equations (Karniadakis, Bullister & Patera 1985).

We give no further description of our numerical techniques here, as this can be found in detail in the references cited above. An example of the accuracy of the method as applied to simulation of Tollmien–Schlichting waves is given below. All results presented here have been confirmed to be convergent in both time-step and spatial degrees-of-freedom, and therefore all solutions discussed are believed to be accurate solutions of the Navier–Stokes equations.

2.3. *Tollmien–Schlichting waves*

We note that, for the choice $a = 0$ (no groove), the general problem described in §2.1 reduces to that of plane Poiseuille flow. Although this 'simple' problem may appear to be irrelevant to the case of finite a, this is, in fact, not the case, and we therefore briefly discuss the stability properties of this flow. As is well known, a solution to the plane-Poiseuille-flow problem is the parabolic profile, $v_s = (1 - y^2)\,\hat{x}$. The linear stability of this flow with respect to infinitesimal disturbances of the form

$$v'(x, t) = \exp(\sigma t)\,\mathrm{Re}\,\{\hat{v}(y)\exp(i\alpha x - 2\pi i\Omega t)\} \qquad (9a)$$

(Tollmien–Schlichting waves of wavelength $2\pi/\alpha$), is governed by the classical Orr–Sommerfeld equation (Drazin & Reid 1981), the least-stable (wall) mode of which we denote

$$\mathscr{F}(\sigma_{\mathrm{TS}}, \Omega_{\mathrm{TS}}, v; \alpha, R) = 0. \qquad (9b)$$

Solution of (9b) using, for instance, spectral methods (Orszag 1971), gives the critical values for the onset of instability ($\sigma > 0$) of $R_{\mathrm{c,TS}} = 5772$, $\alpha_{\mathrm{c,TS}} = 1.02$.

Therefore, for the Reynolds numbers of interest in this paper, $0 < R < 2000$, the parabolic Poiseuille profile is linearly stable ($\sigma < 0$). Furthermore, it has been shown that, even for *finite-amplitude* (two-dimensional) disturbances, the parabolic profile is still stable for this Reynolds-number range, nonlinear instability occurring only
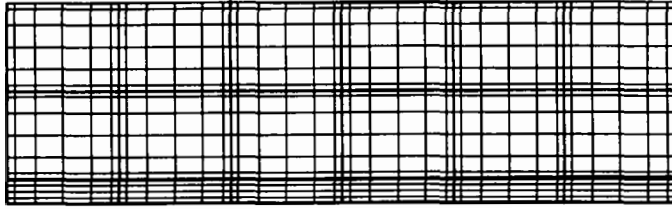
FIGURE 2. A plot of the spectral element mesh used for the direct simulations of Tollmien–Schlichting channel modes. The darker lines correspond to spectral element boundaries, whereas the lighter lines represent the Chebyshev grids internal to a given element. The grouping of points near the bottom wall of the channel is in preparation for the presence of a groove.
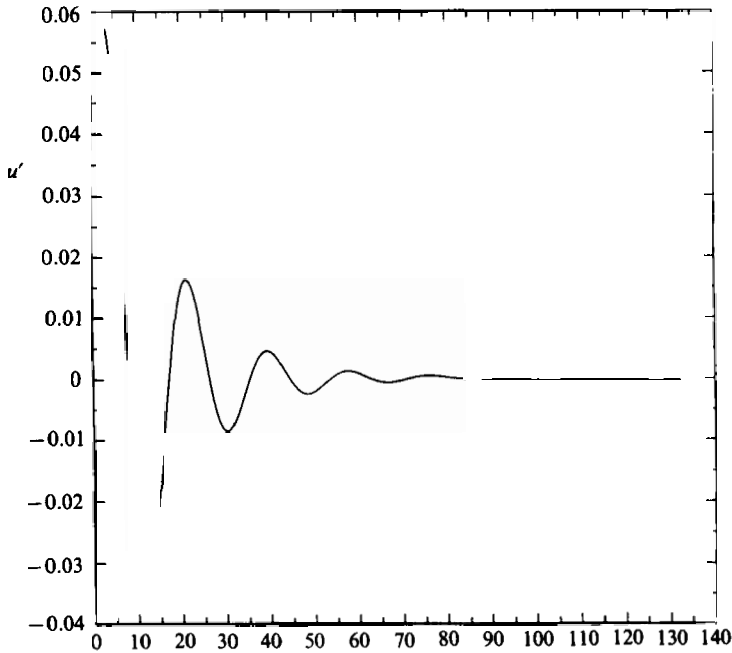
for $R > 3000$ (Herbert 1976). Thus, for the parameters of the present investigation, we conclude that, in the *absence* of a groove, no channel instabilities or unsteadiness should occur.

As an example of both the initial-value-problem philosophy, and the accuracy of our numerical techniques, we consider the decay of the least-stable Tollmien–Schlichting wave in a channel of imposed periodicity length. In particular, we perform a direct simulation of (5) with $v_s = (1 - y^2)\,\hat{x}$, starting with the exact eigenfunction for the least-stable Orr–Sommerfeld mode from (9) as the initial condition $v'(x, t = 0)$. The first test case is $R = 525$, $L = 6.666$ ($m = 1$), for which the least-stable mode corresponds to $\alpha = 0.9424$. The mesh used is shown in figure 2, where the darker lines indicate element boundaries, and the lighter lines are the Chebyshev grids internal
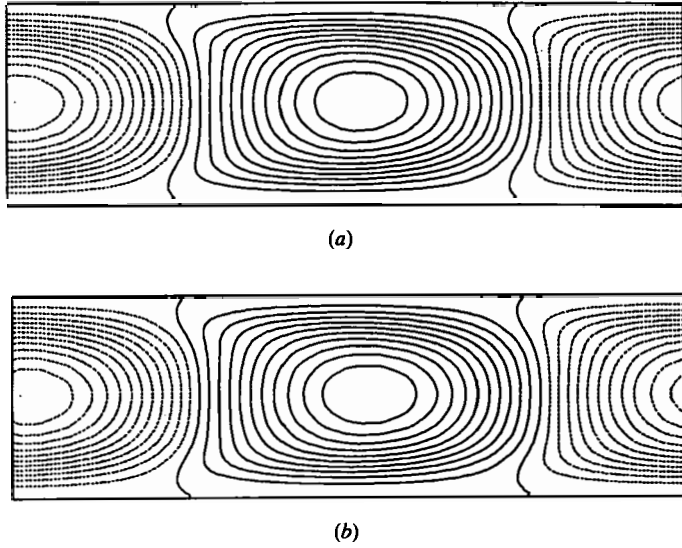
(a)

(b)

FIGURE 4. A plot of the perturbation streamlines at (a) $t = 0$, and (b) $t = T$, for the channel simulations at $R = 525$. The fact that the simulation almost exactly honours the initial (exact) eigenfunction shape is indicative of an accurate numerical solution, with minimal dispersion errors.
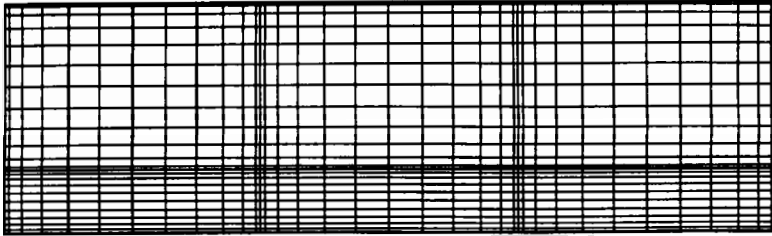

FIGURE 5. A plot of the high-resolution spectral element mesh used for the channel simulations at $R = 1000$. Finer resolution is required at these higher Reynolds numbers in order both to reduce numerical diffusion effects, and to accurately resolve the thinner internal (critical) and boundary layers.

to individual elements. The grouping of elements near the bottom wall is in preparation for the presence of a groove (and associated free shear layer).

We plot in figure 3 the numerical solution for the perturbation velocity u' as a function of time at a representative point in the flow domain. On the basis of this curve and the interpretation (8), the values of the growth rate σ and frequency Ω can be read off as $\sigma = -0.070$, $\Omega = 0.055$, in good agreement with the exact values (obtained from (9)) of $\sigma_{TS} = -0.0695$, $\Omega_{TS} = 0.0546$. In figure 4 we plot the perturbation streamlines at $t = 0$ (exact), and after one time period of simulation, $t = T(= 1/\Omega)$; there is virtually no change in shape, indicating an accurate numerical solution and minimal numerical dispersion.

We now repeat the above test for the slightly more difficult case of $R = 1000$ (all other parameters unchanged), with the higher-resolution mesh shown in figure 5. In figure 6 we plot the perturbation velocity as a function of time, from which we infer $\sigma = -0.044$, $\Omega = 0.051$, again in good agreement with the exact values from (9), $\sigma_{TS} = -0.0459$, $\Omega_{TS} = 0.0503$. It is therefore clear that, at these Reynolds numbers,
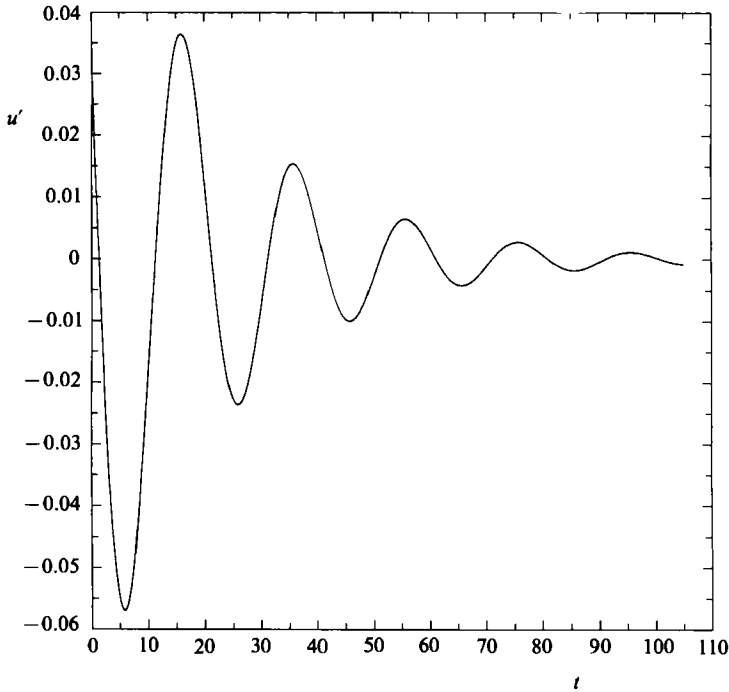
FIGURE 6. A plot of the perturbation velocity u' as a function of time at a typical point in the channel domain shown in figure 5, obtained by direct simulation of the linearized Navier–Stokes equations at $R = 1000$. The initial condition for the simulation is taken to be the Orr–Sommerfeld mode at $R = 1000$ with largest growth rate σ_{TS}.

our numerical methods are sufficiently accurate to handle the relatively delicate test case of a decaying Tollmien–Schlichting wave. As the instability to be discussed below (§4) involves the interaction of a shear layer and a Tollmien–Schlichting wave, accurate solution of the plane Poiseuille problem is a *minimum* requirement for any numerical scheme purporting to simulate the full grooved-channel flow.

3. Steady-state flows

In this section we consider flows that, started from arbitrary initial conditions, converge to a stable steady state. In effect, the results presented here are obtained by iteration of the spectral element discretization of the Navier–Stokes equations (1) to a converged (in time) solution. Our direct simulations are not capable of finding unstable steady states, and we therefore can draw no conclusions concerning their possible existence. The base geometry used in this and the remaining sections corresponds to the choice of parameters $L = 6.6666$, $l = 2.2222$, $a = 1.1111$; the computational domain and a typical spectral element mesh are shown in figure 7. Note that we have included only one groove in the domain, equivalent to the choice of $m = 1$ in $(2b)$ and $(3b)$.

An example of a steady flow at a relatively low Reynolds number, $R = 225$, is shown in figures 8 (a), (b), and (c) in the form of streamline, vorticity and pressure contours respectively. Our pictures are qualitatively the same as previous steady simulations (Pan & Acrivos 1967; Mehta & Lavan 1969; Gatski & Grosch 1984). The formation of a (weak) shear layer at the groove edge, the characteristic (low) high pressure at
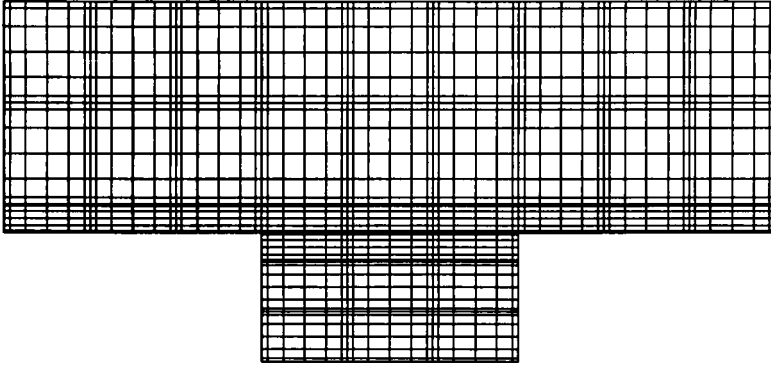
FIGURE 7. The computational domain and a typical spectral element mesh for the grooved-channel calculations in the base geometry $L = 6.6666$, $l = 2.2222$, $a = 1.1111$. Points are crowded near the groove lip so as to accurately resolve the cavity shear layer.

(separation) impingement, and the effect of recirculation on the vorticity distribution in the groove, are all consistent with physical intuition. Note also the almost complete lack of communication between the groove and channel flows, with the latter being very close to a parabolic plane-Poiseuille-flow profile.

We now repeat the above calculation at a larger Reynolds number, $R = 800$, with the resulting streamline, vorticity, and pressure plots shown in figures 9 (a), (b) and (c) respectively. The most noticeable change from the $R = 225$ case is the sharper shear layer, as evinced by rapid vorticity variation across the groove lip. One can also see at this higher Reynolds number the formation of secondary vortices in the corners of the grooves (Pan & Acrivos 1967; Mehta & Lavan 1969; Moffatt 1964). Although of interest in their own right, these (very weak) vortices do not appear to be dynamically significant, and we have not expended the degrees-of-freedom required to resolve them.

In general, for these subcritical (steady-flow) Reynolds numbers, it is found that, for specified flow rate (4), the pressure drop is less than the corresponding quantity for plane Poiseuille flow (i.e. no groove). In particular, we define the quantity Φ to be the ratio of the (time-mean) pressure gradient $\overline{\Pi}_x$ to the corresponding quantity for plane Poiseuille flow $2/R$, $\Phi = \frac{1}{2}\overline{\Pi}_x R$. For these subcritical Reynolds numbers $\Phi \simeq 0.97$, thus showing that the effect of the addition of a groove to a plane channel is one of drag *reduction* and *decreased* dissipation. This is due to stress relaxation and lack of significant momentum flux at the groove lip, and is consistent with experimental observations (Gharib 1984). We discuss dissipation further in §5, in the context of supercritical (oscillatory) flows.

The last point that must be addressed concerning these steady flows is their stability with respect to subharmonic disturbances. In using the computational domain shown in figure 7, we implicitly assume that the periodicity index m in (2b), (3b) is unity. The only way to be certain that these $m = 1$ solutions are physically realizable is to simulate the flow in multi-groove domains (computationally a very expensive procedure), and verify that the L-periodic solutions do, in fact, persist. In figure 10 we show the spectral element mesh for a $m = 2$ calculation, and in figure 11 we show the resulting streamlines at a Reynolds number of 225. Comparing figure 11 with figure 8 (a) it is clear that, for this particular case, the single-groove calculations are justified.
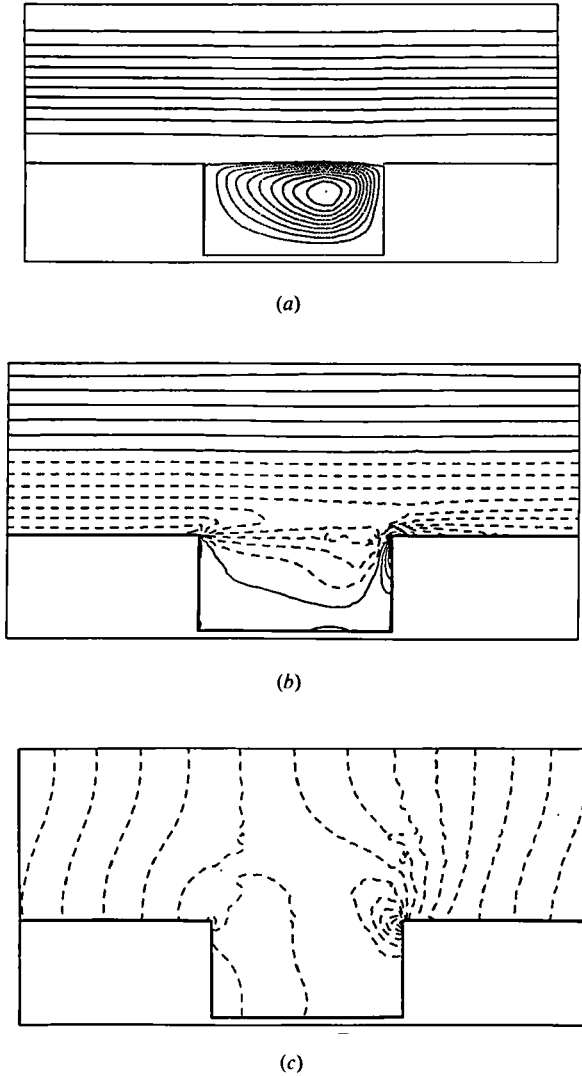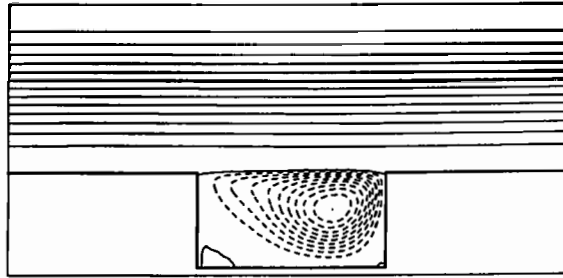
(a)

(b)

(c)

FIGURE 8. Plots of the (a) streamline, (b) vorticity, and (c) pressure contours for steady flow at $R = 225$ in the base geometry. These pictures are consistent with past simulations and visualizations of groove flows.

4. Linear stability theory

4.1. *General stability characteristics*

We now consider the linear stability of the steady flows presented in the previous section. Of interest is the determination of the critical Reynolds number for the onset of unsteadiness, as well as the frequency of oscillation of the corresponding unstable mode. Our linear-theory calculations proceed by direct simulation of (6)–(7), with v_s given by the numerical steady states (perforce stable) calculated in §3. All results in the current subsection are for the base geometry $L = 6.6666$, $l = 2.2222$, $a = 1.1111$.
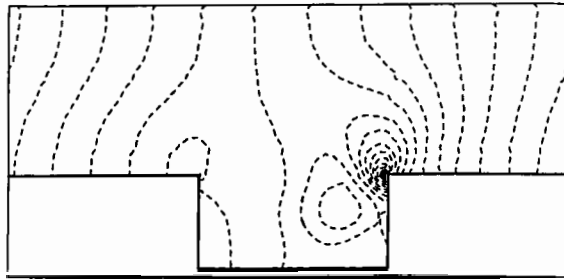
A typical (time-asymptotic) result of a direct simulation is shown in figure 12, which is a plot of the perturbation velocity u' as a function of time for a Reynolds number

(a)
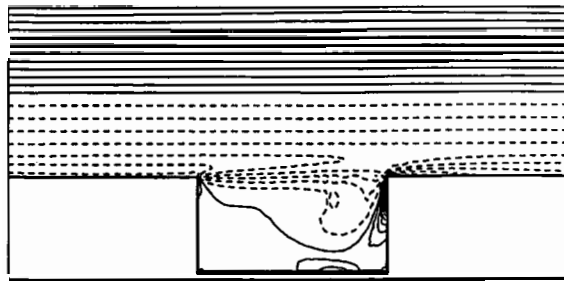
(b)

(c)

FIGURE 9. Plots of the (a) streamline, (b) vorticity, and (c) pressure contours for steady flow at $R = 800$ in the base geometry. At this higher Reynolds number, the cavity shear layer is more pronounced than at $R = 225$.

of $R = 525$. Interpretation of the solution according to (8) gives a growth rate and frequency of $\sigma = -0.043$, $\Omega = 0.142$ respectively. As might be expected from the geometry and flow conditions, the least-stable mode is seen to be oscillatory in nature, consistent with subsequent overstability and self-sustained oscillations.

On the basis of results such as those in figure 12, we plot in figure 13(a) the (σ, Ω)-trajectory of the least-stable mode of the grooved-channel flow, and in figure 13(b) the dependence of growth rate σ on Reynolds number R. Extrapolation of the
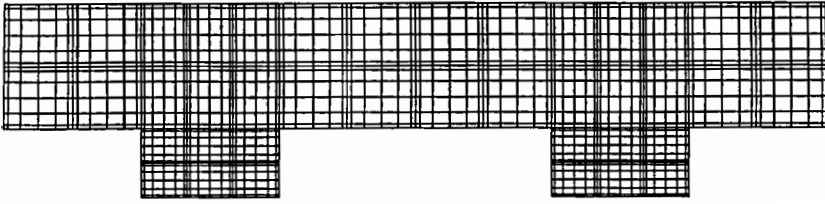
FIGURE 10. A plot of the computational domain and spectral element mesh for a $m = 2$ (two-groove) calculation (base geometry). Periodicity is now required only on the interval $2L$, rather than the more restrictive condition of L-periodicity imposed on single-groove meshes such as that shown in figure 7.
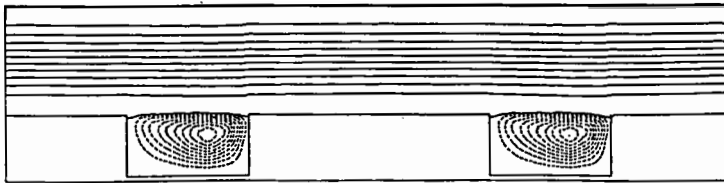

FIGURE 11. A plot of the streamlines of the steady flow for the two-groove domain shown in figure 10 at $R = 225$. The similarity of this picture to that in figure $8(a)$ indicates that, for this particular flow, our L-periodic solutions are stable to subharmonic (two-dimensional) disturbances.
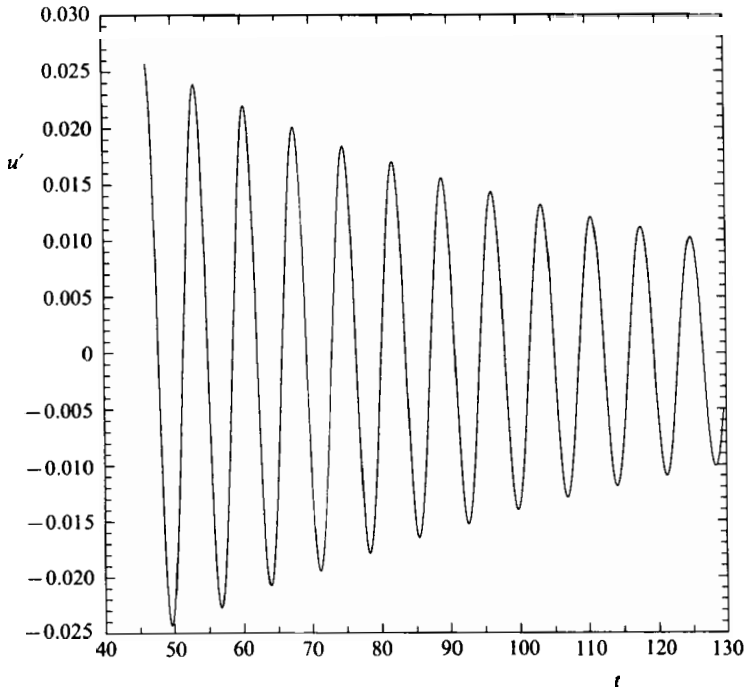

FIGURE 12. A plot of the perturbation velocity u' as a function of time at a typical point in the grooved-channel domain shown in figure 7. obtained by direct simulation of the Navier–Stokes equations at $R = 525$ linearized about a numerically calculated steady state. The decay rate and frequency of the least-stable grooved-channel mode is readily inferred from the (time-asymptotic) behaviour shown here.
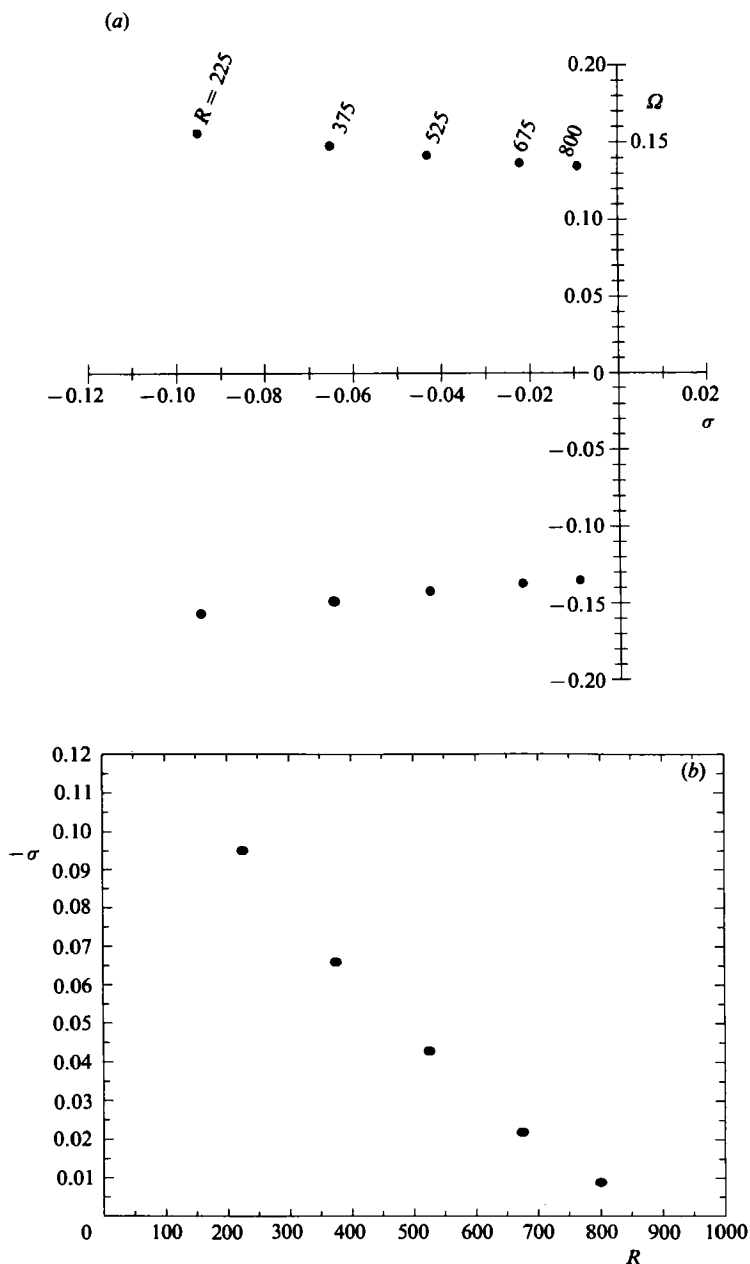
(a)

FIGURE 13. (a) A plot of the (σ, Ω)-trajectory of the least-stable grooved-channel mode, parametrized by the Reynolds number R (base geometry). It is clear that, at a Reynolds number on the order of 1000, the least-stable eigenvalue of the linearized system will pass from the left- to the right-hand plane, and self-sustained flow oscillations will result. (b) A plot of the decay rate of the least-stable grooved-channel mode as a function of Reynolds number R (base geometry). Linear extrapolation of the high-Reynolds-number data points suggests a critical Reynolds number R_c of approximately 900. This estimate will be verified and refined in §5.
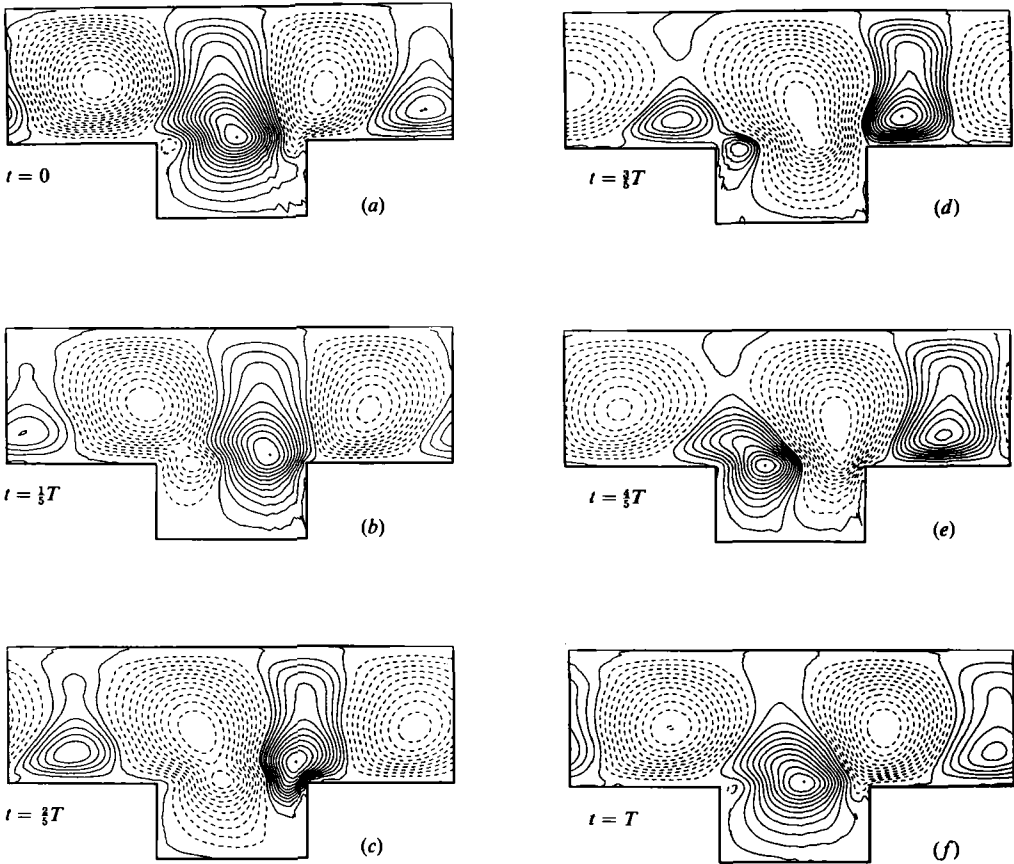
FIGURE 14. A plot of the perturbation streamlines of the least-stable grooved-channel mode at $R = 525$ for various times during the flow cycle, $0 < t < T$ (base geometry). The channel region of the flow closely resembles a $L/2$-periodic Tollmien–Schlichting wave, as can be seen from a comparison with figure 4.

high-Reynolds-number data points in figure 13 (b) clearly predicts instability $(\sigma > 0)$, with a critical Reynolds number R_c of roughly 900. This result will be confirmed and refined in our discussion of nonlinear oscillations in the next section. (Note our present methods can only find stable steady states, and therefore we can formally perform linear-stability calculations only for stable flows.)

To determine the nature of the hydrodynamic instability reflected in figure 13, we plot in figure 14 the perturbation streamlines for $R = 525$ at several times during the flow cycle, $0 < t < T$. (Although the analysis here is for a stable mode, it is clear that the physical features described are similar to their unstable counterparts at slightly higher Reynolds number.) Note that, at $t = T$, the form of the perturbation is almost identical with that at $t = 0$, indicating that we have, indeed, reached a time-asymptotic state in which the solution corresponds to a purified least-stable mode (e.g. (8)). What is most striking in figure 14 is that, in the channel part of the domain, the grooved-channel mode very closely resembles a travelling Tollmien–Schlichting wave (see figure 4), particularly in the region of the flow away from the immediate vicinity of the groove. An even more dramatic comparison between the grooved-channel modes and Tollmien–Schlichting waves is given in the next subsection.
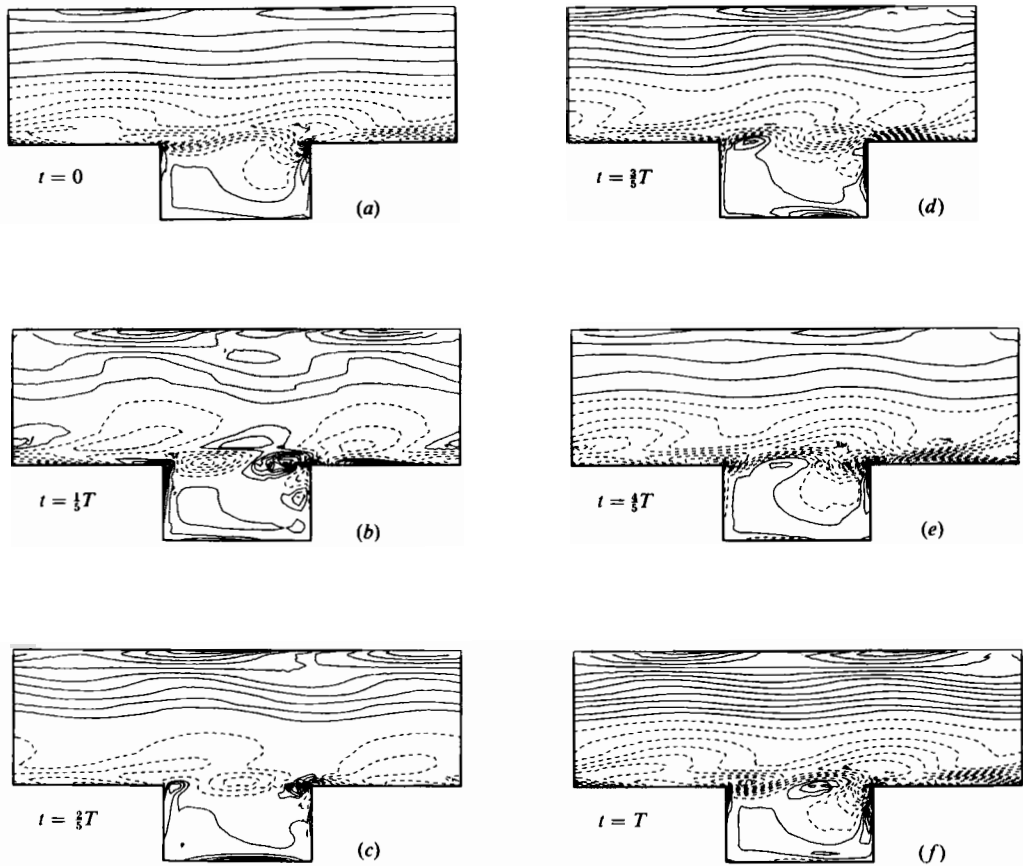
FIGURE 15. A plot of the total vorticity (perturbation field arbitrarily scaled to correspond to maximum velocity of 0.1) for the grooved-channel flow at $R = 525$ for various times during the flow cycle, $0 < t < T$ (base geometry). The waviness of the cavity shear layer is (loosely) suggestive of Kelvin–Helmholtz instability.

It is clear that the Tollmien–Schlichting waves seen in figure 14 cannot be directly responsible for the grooved-channel instability, given the disparity between the linear critical Reynolds number of approximately 900 in figure 13, and the corresponding quantity of $R_{c, TS} = 5772$ for plane Poiseuille flow. (Our numerical tests on decaying Tollmien–Schlichting waves at $R = 1000$ in §2.3 should be ample proof that the instabilities seen here are *not* the result of inaccurate channel-flow simulation.) In order to isolate the mechanism by which the groove region destabilizes the flow, we plot in figure 15 contours of the total vorticity $\omega_s + \epsilon\omega'$, at various times during the flow cycle, $0 < t < T$. The amplitude of the perturbation ϵ is (arbitrarily) chosen to correspond to a maximum perturbation velocity of roughly 10%. As might be expected, there is significant waviness and 'roll-up' of the vortex sheet at the groove lip (as compared with the steady case, figure 9b), strongly suggestive of similar patterns observed in Kelvin–Helmholtz instability of free shear layers (e.g. Michalke 1964). In summary, it is clear from figures 14–15 that the grooved-channel instability is a complex interaction between a destabilizing cavity shear layer, and 'stable' Tollmien–Schlichting waves in the channel interior.

4.2. *Frequency selection – geometric dependence*

In this section, we present a very simple theory for predicting the frequency Ω of the least-stable mode of a grooved-channel flow. Understanding the linear frequency selection process can be important for several reasons. First, the behaviour of forced grooved-channel flow is easily predicted once the characteristic response of the unforced flow is understood; see Part 2 of this paper (Ghaddar, Magen, Mikic & Patera 1985) for an application of resonant forcing to heat-transfer enhancement. Secondly, the frequency of the nonlinear (supercritical) oscillations is typically only slightly shifted from that of the originating linear instability, and we can therefore use linear analysis to predict less tractable nonlinear behaviour.

From the pictures and arguments presented in the previous section, it appears reasonable to interpret the grooved-channel instability process as free-shear-layer destabilization of erstwhile stable Tollmien–Schlichting waves. If this were the case, it also seems plausible that the unstable part of the flow, the shear layer, would allow the stable, 'massive' part of the flow, the Orr–Sommerfeld mode, dictate the frequency of their coherent oscillations, in this way minimizing the resistive component of the system. Equivalently, one can view the instability process as broadband shear-layer instability, with the least-stable mode of the 'coupled' system then corresponding to the frequency at which the channel modes are least damped.

These rather simple frequency-selection scenarios, which predict $\Omega = \Omega_{\mathrm{TS}}$, turn out, in fact, to be correct. To illustrate how the theory is implemented, we consider the particular case of the base geometry $L = 6.6666$, $l = 2.2222$, $a = 1.1111$, at $R = 525$, for which the linear-theory direct-simulation results are given in figures 14 and 15. In order to be able to calculate Ω_{TS} from (9), we must know the correct wavenumber α of the Tollmien–Schlichting wave associated with the grooved-channel mode. Although the boundary condition of L-periodicity (2b) restricts the wavenumber to be of the form $\alpha = 2\pi n/L$, n integer, the value of n is not known *a priori*. We therefore resort to the direct-simulation results, figure 14, from which we deduce that $n = 2$, and hence $\alpha = 1.885$. Solution of (9) then gives $\Omega_{\mathrm{TS}} = 0.146$, in excellent agreement with the simulation result for the grooved channel $\Omega = 0.141$.

To give an indication of the large effect of geometry on frequency selection, we now consider the case of $L = 5.185$, $l = 2.2222$, $a = 1.1111$, still at $R = 525$. This geometry is identical to the base geometry, except for a 20 % decrease in periodicity length L. To determine n for this new geometry, we plot in figure 16 the perturbation streamlines at several times during the flow cycle, analogous to figure 14 for $L = 6.6666$. (Note once again the remarkable resemblance of the grooved-channel mode to the Tollmien–Schlichting wave in figure 4.) From figure 16 it is clear that for this shorter geometry $n = 1$, which in turn gives a wavenumber of $\alpha = 1.211$ for the associated Tollmien–Schlichting wave. With these parameters, (9) gives $\Omega_{\mathrm{TS}} = 0.081$, which is, once again, in good agreement with the direct-simulation results for the grooved channel, $\Omega = 0.083$. Because of the two-wave ($n = 2$) to one-wave ($n = 1$) transition, a slight decrease in domain length ($L = 6.6666$ to $L = 5.185$) is seen to result in a large change in frequency ($\Omega = 0.141$ to $\Omega = 0.083$). Although it might appear that this geometric sensitivity is forced on the solution by the single-groove ($m = 1$) simulations, this does not appear to be the case. Two-groove ($m = 2$) simulations for these geometries indicate that, as for the steady flow in figure 11, our L-periodic solutions persist despite the freedom of a larger domain.

The fact that we can easily vary the geometry of the grooved channel allows us to verify the Tollmien–Schlichting wave theory in a fairly exhaustive fashion. In
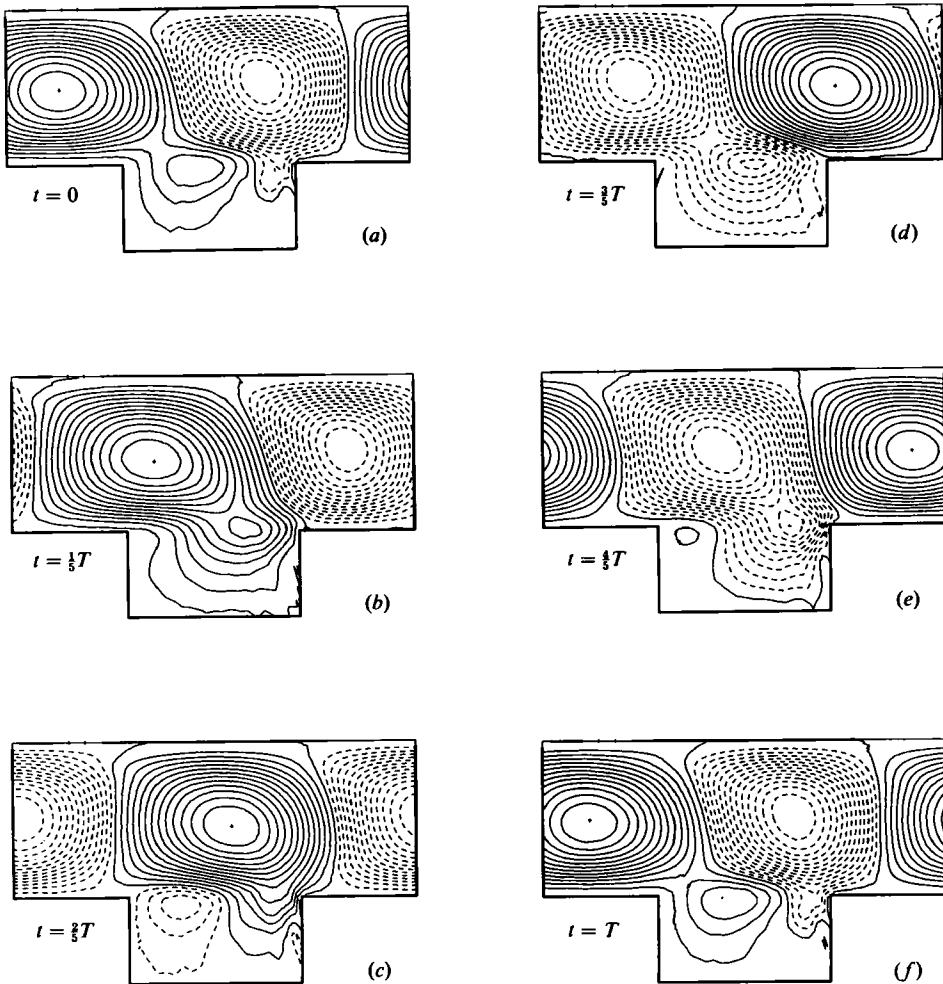
FIGURE 16. A plot of the perturbation streamlines of the least-stable grooved-channel mode at $R = 525$ for various times during the flow cycle, $0 < t < T$, for the geometry $L = 5.185$, $l = 2.2222$, $a = 1.1111$. The resemblance of the channel region of the flow to a Tollmien–Schlichting wave is even more striking for this $n = 1$ (one-wave) solution than for the two-wave solution in figure 14.

figure 17 we collapse all the frequency data from numerous geometries on the dispersion relation for the least-stable wall mode of the Orr–Sommerfeld equation (9), in which each data point is the result of an analysis similar to that described in the previous two paragraphs. For this range of parameters, the theory is seen to be virtually exact. In table 1 we list the various geometries appearing in figure 17, grouped into three categories based on common values of l. Independent tests have verified that the frequency is not a function of groove depth a and we have therefore only included variations in L and l.

The remaining point to be resolved is the possibility of *a priori* prediction of n, the number of Tollmien–Schlichting waves per periodicity length. In figure 18, we plot frequency Ω as a function of L/l, for three values of l. (It should be noted that, for very large values of l, the theory presented here certainly breaks down, as the
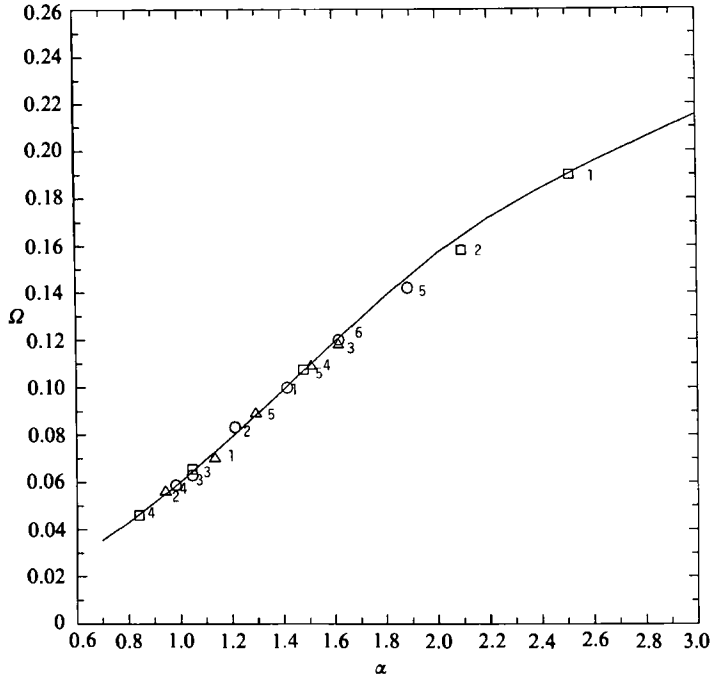
FIGURE 17. A plot of the frequencies Ω for the various geometries studied *versus* the wavenumber of the associated Tollmien–Schlichting channel waves α at a Reynolds number of $R = 525$. All the points are seen to fall almost exactly on the Orr–Sommerfeld dispersion relation, indicating that the frequency-selection process is ultimately dictated by the more stable 'component' of the system, the channel flow. Data is grouped by $\square_i$ for geometries with $l = 1.5$, $\bigcirc_i$ for geometries with $l = 2.22$, and $\triangle_i$ for geometries with $l = 2.77$; the subscripts refer to variations in L (for given l), and are explained in table 1.

shear layer will in this case re-attach before the downstream groove face, resulting in a very different, grossly non-parallel, flow structure. For this reason, we restrict ourselves to small and moderate l, corresponding to 'open' cavities.) We first consider the case of $l = 1.5$, which is typical of our results for small l. In this small-groove limit, there is little groove/channel interaction, and the transition from one wave to two waves is governed primarily by the stability of the channel flow. In other words, the two-wave transition in figure 18 can be shown to roughly correspond to maximization of σ_{TS} ($\alpha = 2\pi n/L$) with respect to n. It should also be noted that, for this low value of l, the decay rates of the grooved-channel modes, σ, are quite close to those of the associated Tollmien–Schlichting waves σ_{TS}, suggesting that the effect of the groove on the stability of the flow is relatively small.

At larger values of l ($l = 2.22$, 2.77 in figure 18), the transition from one wave to two waves is roughly correlated with a critical value of L/l. For these larger grooves the Tollmien–Schlichting wave chosen is often *not* the least stable mode consistent with L-periodicity, indicating that an important factor now is geometric compatibility between the groove and channel oscillations. Also, the decay rates of the grooved-channel modes are now much less than the corresponding plane-channel modes, evidence of strong interaction between the free shear layer and the Tollmien–Schlichting waves in the channel. For instance, for the base geometry, the $n = 1$ Tollmien–Schlichting wave has a decay rate $\sigma_{TS} = -0.070$, the $n = 2$ wave (which

	i	l	L	Ω	n
□	1	1.5	2.5	0.19	1
	2		3.0	0.154	1
	3		6.0	0.065	1
	4		7.5	0.046	1/2
	5		8.5	0.108	2
○	1	2.22	4.44	0.1	1
	2		5.185	0.083	1
	3		6.0	0.064	1
	4		6.4	0.059	1
	5		6.66	0.142	2
	6		7.77	0.12	2
△	1	2.77	5.54	0.07	1
	2		6.66	0.056	1
	3		7.77	0.118	2/1
	4		8.33	0.109	2
	5		9.72	0.089	2

TABLE 1. A table listing the various geometries represented in figures 17 and 18, giving L, l, Ω (at $R = 525$) and n for each geometry. The groove depth in all cases is $a = 1.1111$.

is the case actually realized in the grooved channel, i.e. the associated wave) has decay rate $\sigma_{TS} = -0.12$, while the grooved-channel mode has decay rate $\sigma = -0.043$. Note this is not to say that the stability of the channel modes is unimportant. For instance, for the geometry $L = 5.185$, $l = 2.2222$, $a = 1.1111$, we find that $\sigma = -0.021$, with σ_{TS} (of the associated Tollmien–Schlichting wave) $= -0.0629$. In comparing these numbers to those for the base geometry, it is reasonable to conclude that at least part of the decreased stability of the $L = 5.185$ geometry is due to the slower decay of its associated Tollmien–Schlichting waves. In summary, the determination of the wavenumber (spatial scale) of the linear modes is a complicated function of shear-layer and channel-mode interaction; however, once α is known, the channel dispersion relation governs the frequency of oscillation.

In our discussion of how the wave index n is selected by the system, we have raised the issue of relative stability and geometric dependence of R_c. In this paper, we do not attempt a comprehensive study of this aspect of the stability problem, having rather focused on the frequency characteristics. It is evident from the above results that a shear-layer/Tollmien–Schlichting model for criticality could be constructed analogous to the current frequency model. However, it is also clear that any theory for stability would be more complicated than a theory for frequency, in that determination of the growth rates of the grooved-channel system appears to involve much more intimate coupling between the shear layer and Tollmien–Schlichting waves than determination of frequency, which we have shown is largely (but not entirely) governed by the 'channel side' of the flow. In particular, a stability theory would certainly require a more sophisticated analysis of the shear-layer structure than the rather cursory treatment given in §4.1.

We briefly discuss to what extent the frequency and stability characteristics described here are observed experimentally. Since no experimental results exist for the same conditions we have studied (with the exception of heat-transfer data related to Part 2 of this paper (Ghaddar, Greiner, Patera & Mikic 1985; Greiner 1985)), our
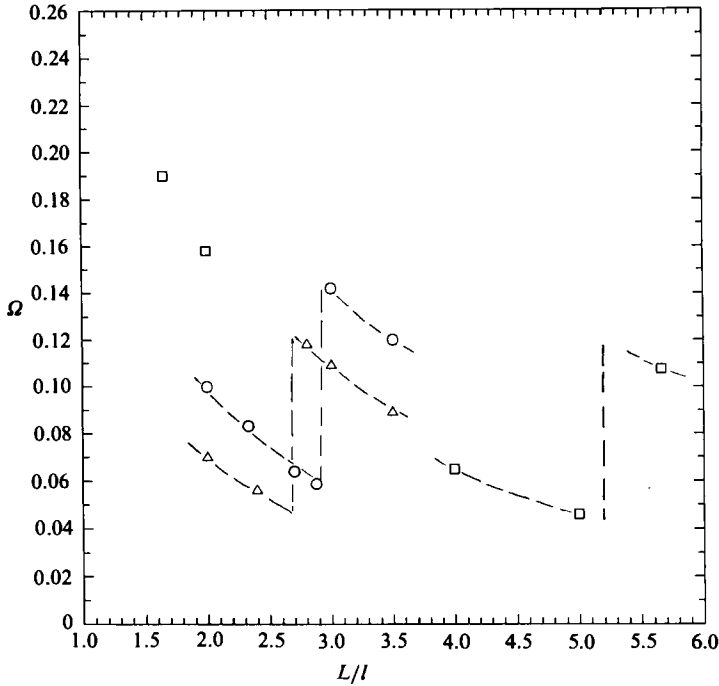
FIGURE 18. A plot of the frequency Ω as a function of L/l, at a Reynolds number of $R = 525$, for three values of l; $\square$, $l = 1.5$; $\bigcirc$, 2.22; $\triangle$, 2.77. The discrete jumps in frequency correspond to transitions from one-wave to two-wave solutions.

comparisons are of necessity qualitative. First, we find that the groove depth is irrelevant to frequency determination, in agreement with the experimental results for boundary-layer flow over grooves (Sarohia 1977). Secondly, we find that, for small grooves (i.e. small l), the groove does not significantly affect the stability of the flow, but that the flow experiences decreasing stability with increasing l; this, too, is seen in boundary-layer groove flows (Sarohia 1977). Lastly, the discontinuous frequency curves shown in figure 18 are observed in a large number of oscillatory separated flows (Sarohia 1977; Rockwell & Naudascher 1979), in which variation of a geometric parameter results in discrete frequency transitions.

Although our (unstable) shear-layer/(stable) channel-mode theory does predict a number of features observed experimentally in a variety of impinging shear-layer flows, this is certainly not conclusive proof that the model is capturing all the relevant physics. However, for isolated grooves, boundary-layer flows, slit flows, even channel expansions (where natural oscillations have been numerically predicted; Osswald, Ghia & Ghia 1983), it seems possible that our theory, appropriately modified for flow and boundary conditions, would still apply. Further numerical tests are currently under way to determine to what extent the unstable shear-layer/stable outer flow decomposition is applicable to these more general groove-like flows. One thing that is clear, at least for the current geometry, is that the use of concepts such as 'Biot–Savart feedback' to explain incompressible oscillations (Rockwell 1982) is, at best, misleading, and certainly an incomplete description of the kinds of phenomena described in this paper. Furthermore, it would appear that any theory for frequency for these flows must include the effect of the outer flow, which is at variance with

most current theories (Rockwell & Naudasher 1979) based solely on shear-layer considerations.

5. Self-sustained oscillations

We now consider the nonlinear evolution of the linear instability predicted in the last section. We are interested in refining the value of R_c predicted by linear theory (figure 13 b), determining the (nonlinear) frequency of oscillation Ω_n, predicting the dependence of the amplitude of the oscillations on degree of criticality $R - R_c$, and understanding the effect of natural oscillation on global flow properties such as dissipation. All results are for the base geometry $L = 6.6666$, $l = 2.2222$, $a = 1.1111$, and are obtained by direct simulation of the (nonlinear) Navier–Stokes equations (1) on the high-resolution spectral element mesh shown in figure 19.

Typical simulation results are shown in figure 20 (a) and (b), which are plots of the (total, not perturbation) streamwise velocity u as a function of time for Reynolds numbers of $R = 800$ and 1200 respectively. In figure 20 (a) we see decay to steady state, as predicted by the linear-theory results of the last section, figure 13 (b). However, in figure 20 (b), at $R = 1200$, it is clear that the stable flow is now not steady, but rather a limit cycle corresponding to a nonlinear self-sustained flow oscillation. On the basis of results such as those in figure 20 for Reynolds numbers in the range $800 < R < 1200$, the critical Reynolds number for the onset of unsteadiness is found to be $R_c = 975$, in reasonable agreement with the linear extrapolation of the linear-theory results in figure 13.

The primary frequency of the nonlinear oscillations Ω_n is, as in the linear case, quite insensitive to Reynolds number R over the narrow range of Reynolds numbers investigated here. For our base geometry, we find from figure 20 (b) that $\Omega_n = 0.141$, which is very close to the frequency of the originating linear mode (see §4) of $\Omega = 0.142$. Thus, at least for small amplitudes, it is clear that the linear frequency theory developed in §3, is, indeed, relevant to the case of self-sustained nonlinear oscillations. This has been verified for geometries other than the base case presented here.

To understand the nature of the nonlinear oscillations, we plot in figures 21, 22, and 23 the streamline, vorticity, and pressure contours respectively of the flow oscillations at $R = 1200$ for various times during the flow cycle, $0 < t < T$ $(= 1/\Omega_n)$. As in the case of the linear modes, we see that the nonlinear oscillations correspond to intense shear-layer activity at the groove lip, which in turn drives a travelling-wave disturbance in the channel interior. The vortex roll-up and pressure signature at the cavity edge are, once again, suggestive of classical Kelvin–Helmholtz instability.

To see more clearly the form of the travelling-wave disturbance in the channel, we go into the wave frame of reference, $x' = x - ct$ $(u' = u - c)$, $y' = y$ $(v' = v)$, $t' = t$, where $c = 2\pi\Omega_n/\alpha$ is the phase speed of the channel wave. Here α is the primary wavenumber of the nonlinear channel disturbance $\alpha = 2\pi n/L$, where n is the non-linear version of the wave index discussed in §4.2. Inspection of figure 23 (say) reveals a two-wave $(n = 2)$ solution, consistent with the structure of the least-stable linear subcritical mode for this geometry (see figure 14). In figure 24, we plot the streamlines of the flow at $R = 1200$ in the wave frame in the channel part of the domain at several times during the flow cycle. First, note that the flow is, indeed, roughly invariant in the proposed wave frame (with the exception of the immediate vicinity of the groove), proof of the travelling-wave nature of the channel solution. Second, the grooved-channel travelling wave is seen to closely resemble a nonlinear Tollmien–Schlichting wave (Herbert 1976; figure 1 in Orszag & Patera 1983), indicating that
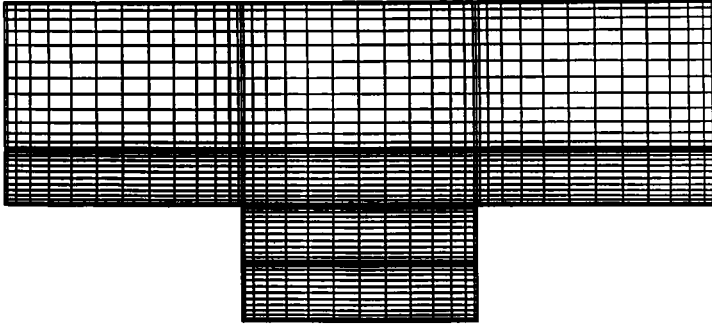
FIGURE 19. The high-resolution spectral element mesh used for simulation of supercritical flows. All results are for the base geometry ($L = 6.6666$, $l = 2.2222$, $a = 1.1111$) shown here.
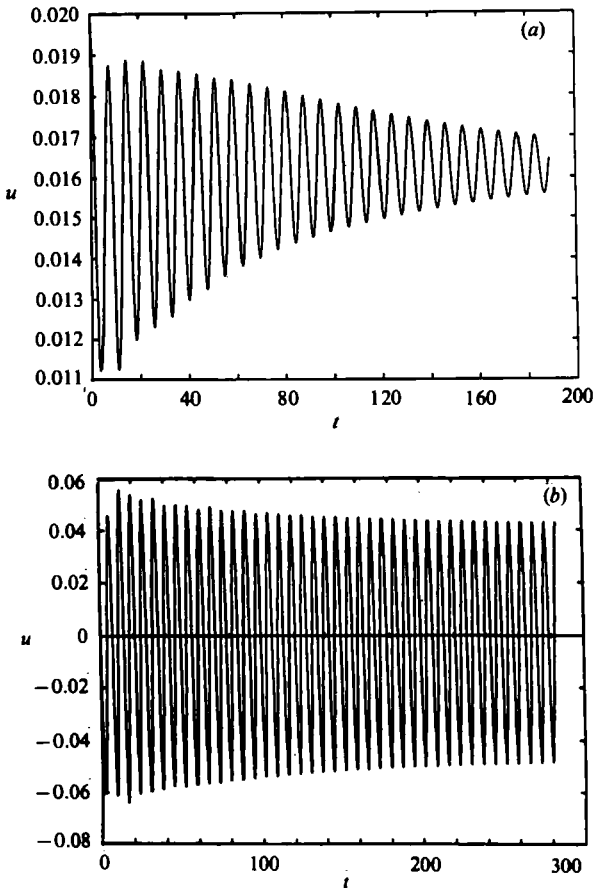

FIGURE 20. A plot of the velocity u as a function of time at a typical point in the flow domain shown in figure 19, obtained by direct numerical simulation of the Navier–Stokes equations (a) Reynolds number $R = 800$; the flow is seen to approach a stable steady state. (b) $R = 1200$; the stable time-asymptotic flow is now not steady but, rather, a limit cycle of frequency $\Omega_n = 0.141$.
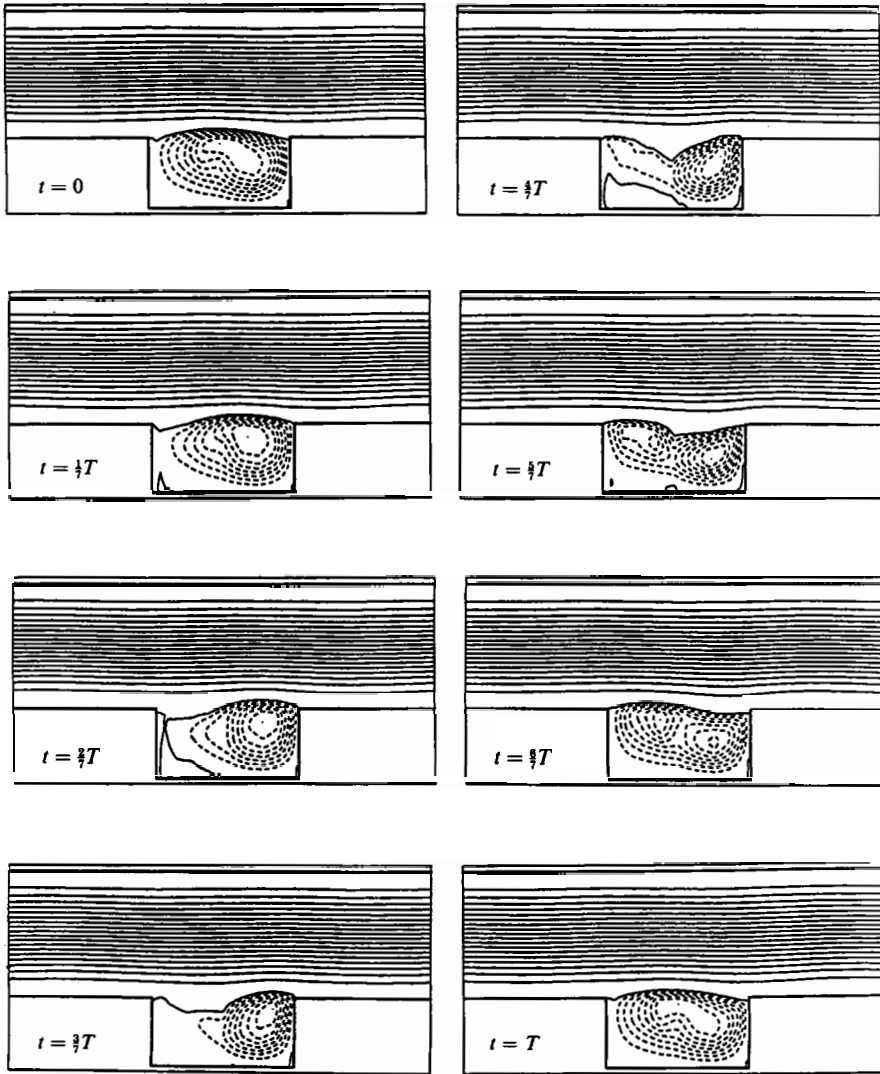
FIGURE 21. A plot of the streamlines of the self-sustained flow oscillation at $R = 1200$ for various times during the flow cycle, $0 < t < T$ (base geometry).

the shear-layer/channel-flow interpretation of the flow does, in fact, extend to the nonlinear problem.

We now turn to an investigation of more global measures of the self-sustained oscillations. To determine the dependence of the oscillation amplitude on degree of criticality, we define a pointwise amplitude parameter, $A_m(x) = \max_t |u(x,t) - \bar{u}(x)|$, where an overbar denotes a time average. In figure 25, we plot this amplitude parameter at a typical point in the flow domain, as a function of Reynolds number R. The curve suggests a square-root dependence,

$$A_m \sim c(R - R_c)^{\frac{1}{2}} \quad (R \to R_c) \tag{10}$$

(c a constant), behaviour typically associated with a regular Hopf bifurcation (Drazin
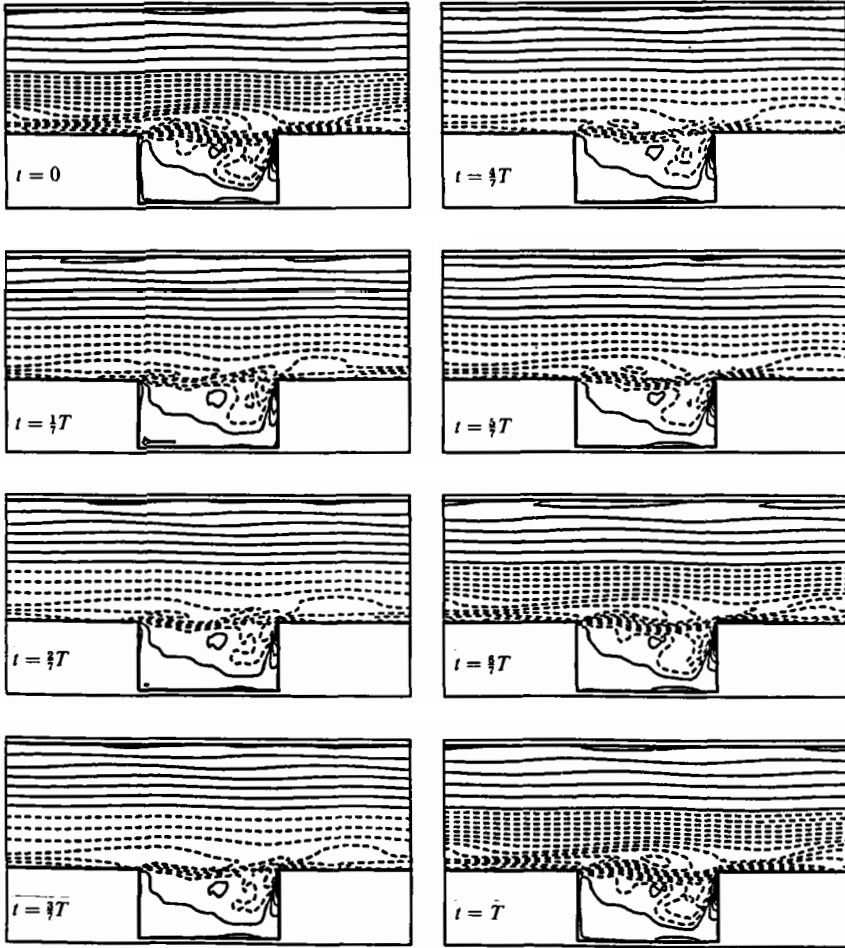
FIGURE 22. A plot of the vorticity contours of the self-sustained flow oscillation at $R = 1200$ for various times during the flow cycle, $0 < t < T$. Note the waviness and roll-up patterns in the free shear layer at the cavity edge.

& Reid 1981). To motivate this behaviour for our particular system, we begin with a Landau amplitude equation (Landau & Lifshitz 1959; Drazin & Reid 1981)

$$A_t = (\sigma + 2\pi\mathrm{i}\Omega) A - \gamma A |A|^2 + ..., \qquad (11a)$$

where A can be thought of as the amplitude of the least-stable mode of the linearized system (see §4), and $(\sigma + 2\pi\mathrm{i}\Omega)$ the corresponding eigenvalue (see figure 13a). Upon multiplying (11a) by A^* (complex conjugate) and taking the real part, we arrive at

$$\tfrac{1}{2}|A|_t^2 = \sigma |A|^2 - \gamma_\mathrm{r} |A|^4, \qquad (11b)$$

where γ_r is the real part of the Landau constant γ. From figure 13(b) it appears that, for our particular system, $\sigma \sim c(R - R_\mathrm{c})$ as $R \to R_\mathrm{c}$. If we then assume that $\gamma_\mathrm{r} > 0$, we find that (11b) predicts equilibria of the form $|A| \sim c \, (R - R_\mathrm{c})^{\frac{1}{2}}$, from which the pointwise dependence (10) then follows.

To determine more precisely the extent to which (10) is realized for our flow, we
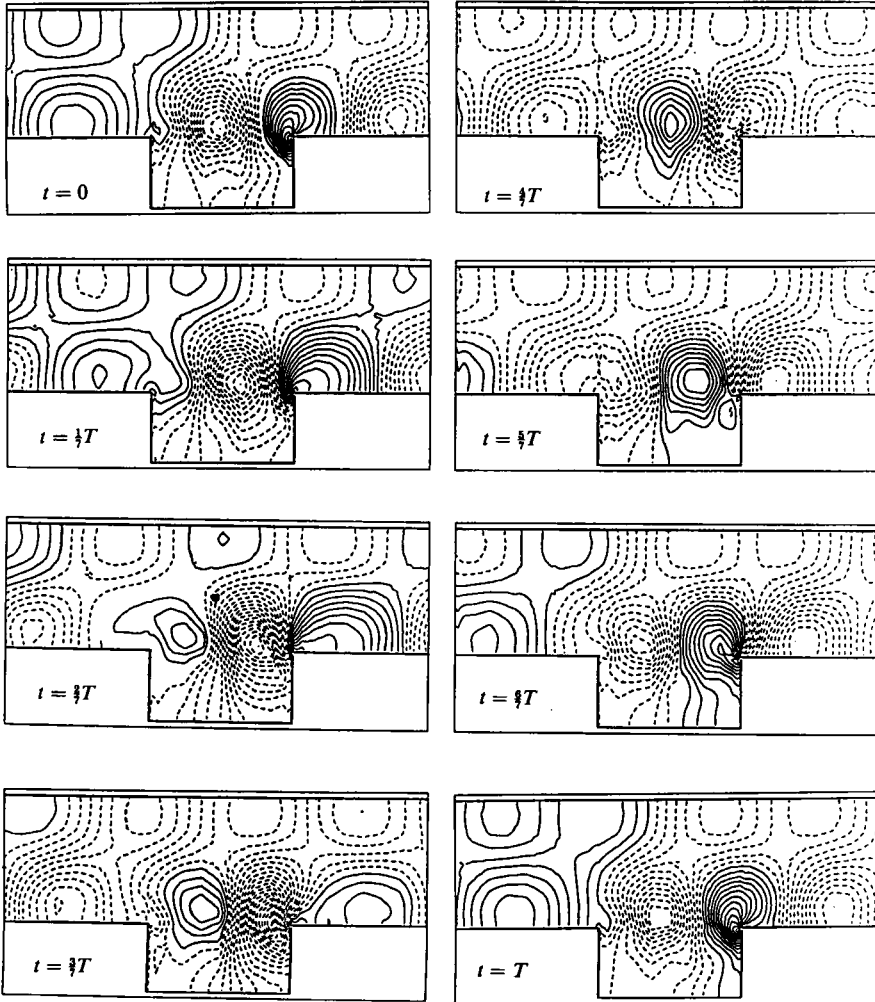
FIGURE 23. A plot of the pressure contours of the self-sustained flow oscillation at $R = 1200$ for various times during the flow cycle, $0 < t < T$. Note the propagating pressure pulse across the cavity shear layer (correlated with the streamline pattern in figure 21), suggestive of shear-layer instability. The two-wave nature of the channel solution can easily be seen in the pressure patterns.

have done a least-squares fit on $\ln A_m = a \ln (R - R_c) + b$ (parameters a, b) for the particular point in the flow domain corresponding to figure 25. This analysis gives $a = 0.48275$, $b = -5.69392$, with a correlation coefficient (for $\ln A_m$, $\ln (R - R_c)$) of 0.99961. This is strong evidence in support of the square-root dependence in (10). We have plotted the result of this fit on figure 25, where it is seen that, as expected, the agreement is quite good.

Thus, we have shown numerically that the self-sustained groove oscillations observed experimentally are the result of a regular Hopf bifurcation, corresponding to simple crossing (figure 13b) of a pair of complex-conjugate eigenvalues from the left- to right-hand stability plane (figure 13a). In obtaining this result we have, of course, neither derived not solved the Landau equation (11). The purpose of presenting the Landau arguments is to show how direct simulation even of
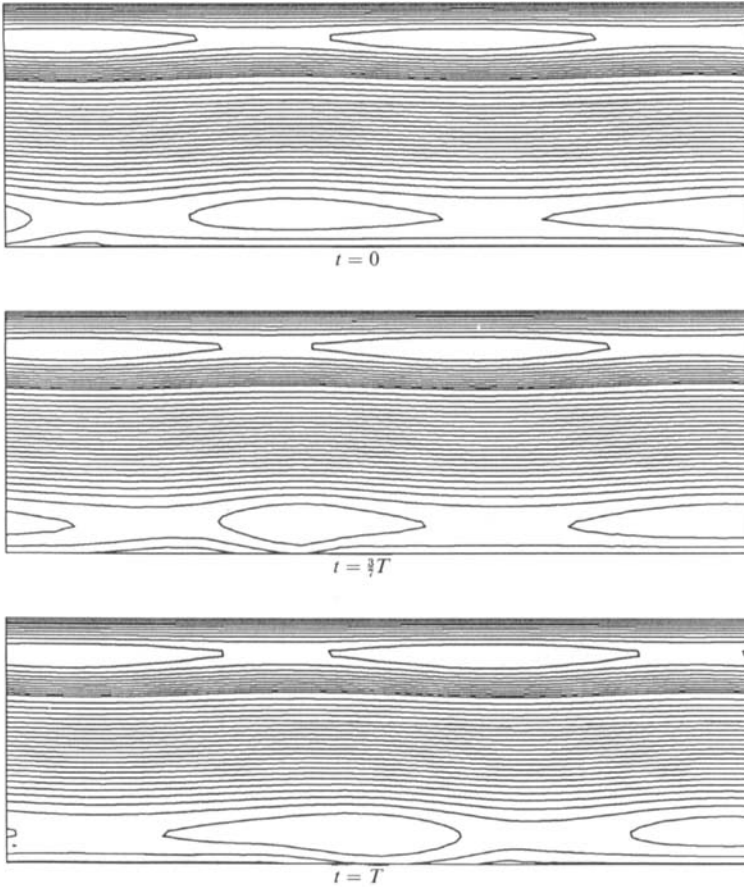
FIGURE 24. A plot of the streamlines in the wave frame, $x' = x - ct$, $y' = y$, $t' = t$, where $c = 2\pi\Omega_n/\alpha$ is the phase speed of the associated channel wave, $c = 0.47$. (This large phase speed for a wall mode is due to the relatively low Reynolds number of the flow.) The flow is, in fact, steady in the proposed wave frame, and closely resembles the finite-amplitude secondary flows seen in plane Poiseuille flow.

complicated flows can be analysed and interpreted in the framework of classical stability theory, in this way extending the theory to a much broader class of flow problems.

Lastly, we reconsider the effect of groove addition on dissipation and drag in a plane channel. In figure 26, we plot the non-dimensional pressure gradient ratio $\Phi = \frac{1}{2}\bar{\Pi}_x R$ over the range of Reynolds numbers $800 < R < 1200$. As discussed in §3, for subcritical R, Φ is less than unity and roughly constant at $\Phi = 0.973$, owing to stress relaxation and negligible momentum flux at the groove lip. Slightly above $R = R_c$, however, the Reynolds stress due to flow oscillation overtakes the stress relaxation effect, and Φ increases above unity. Furthermore, it is seen that $\Phi \sim c(R - R_c)$, $R \to R_c$, which is consistent with the square-root amplitude dependence seen in figure 25, and the fact that the Reynolds-stress term responsible for the increased drag is quadratic in amplitude. Thus, as might be expected, the occurrence of natural flow oscillations is seen to result in significant increased drag and dissipation.
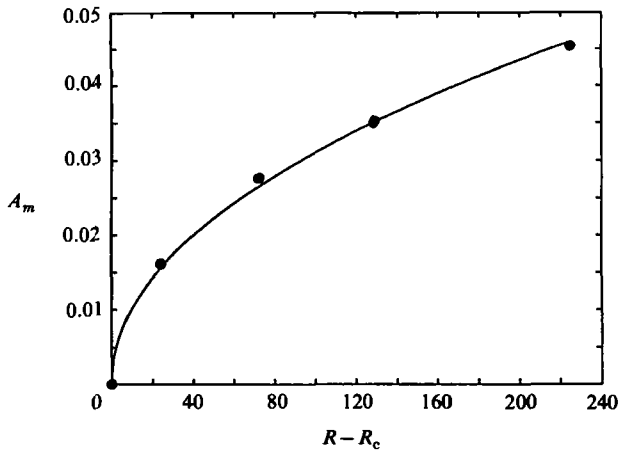
FIGURE 25. A plot of the amplitude of the self-sustained oscillations as a function of Reynolds number R. Also plotted is the least-squares fit to a square-root dependence, the good agreement indicative of a regular Hopf bifurcation.
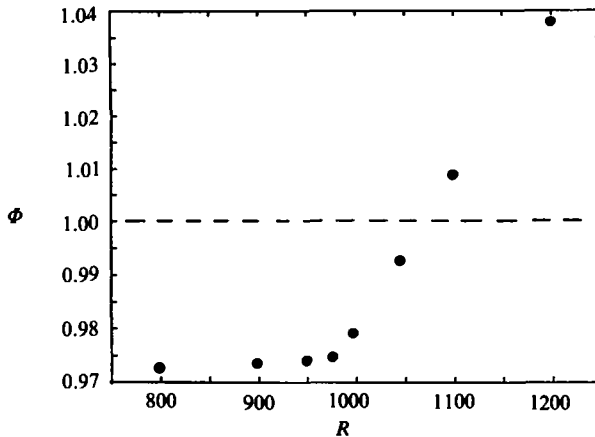

FIGURE 26. A plot of the pressure gradient ratio Φ as a function of Reynolds number R. For subcritical flows, the pressure drop for the grooved channel is less than that for the corresponding planar channel ($\Phi < 1$), owing to stress relaxation at the groove lip. For supercritical flows, the Reynolds stress at the groove lip counteracts the stress-relaxation effect, resulting in (linearly) increasing drag and dissipation.

The close relationship of the linear and nonlinear grooved-channel disturbances to their plane channel (Tollmien–Schlichting) counterparts, suggests that the final transition process in these grooved-channel flows may be quite similar to the three-dimensional secondary instability phenomenon seen in plane Poiseuille flow (Orszag & Patera 1983). Future work will address the three-dimensional transition problem for flow in grooved channels (Ghaddar & Patera 1985), as well as determine the extent to which the stability and frequency theories presented here for groove flows can be extended to more general geometries.

REFERENCES

ARVIZU, D. E. & MOFFATT, R. J. 1982 Experimental heat transfer from an array of heated cubical elements on an adiabatic channel wall. *Rep. No.* HMT-33, Thermosciences Div. Stanford University, Stanford, California.

BABUSKA, I. & DORR, M. R. 1980 Error estimates for the combined h and p versions of the finite element method. *Numer. Maths* **37**, 257.

BASDEVANT, C., DEVILLE, M. O., HALDENWANG, P., LACROIX, J. M., ORLANDI, P., OUAZZINI, J., PATERA, A. T. & PEYRET, R. 1985 Spectral and finite difference solutions of the Burgers equation. *Computers and Fluids* (to appear).

DELVES, L. M. & HALL, C. A. 1979 An implicit matching procedure for global element calculations. *J. Inst. Maths Applics* **23**, 223.

DRAZIN, P. G. & REID, W. H. 1981 *Hydrodynamic Stability.* Cambridge University Press.

DURBIN, P. A. 1984 Resonance in flows with vortex sheets and edges. *J. Fluid Mech.* **145**, 275.

GATSKI, T. B. & GROSCH, C. E. 1984 Embedded cavity drag in steady and unsteady flows. *AIAA Paper No.* 84-0436.

GHADDAR, N. K., GREINER, M., PATERA, A. T. & MIKIC, B. B. 1985 Heat transfer enhancement by oscillatory perturbation of a stable separated flow. *Intl Comm. Heat Mass Transfer* **12**, 369.

GHADDAR, N. K., KARNIADAKIS, G. E. & PATERA, A. T. 1985 A conservative isoparametric spectral element method for forced convection; application to fully-developed flow in periodic geometries. *Numer. Heat Transfer* (to appear).

GHADDAR, N. K., MAGEN, M., MIKIC, B. B. & PATERA, A. T. 1986 Numerical investigation of incompressible flow in grooved channels. Part 2: Resonance and heat transfer enhancement. *J. Fluid Mech* (to appear).

GHADDAR, N. K. & PATERA, A. T. 1985 Stability and resonance in grooved-channel flows. In *Proc. ICASE/NASA Langley Workshop on Stability of Time Dependent and Spatially Varying Flows, Hampton, Virginia,* to appear.

GHARIB, M. 1983 The effect of flow oscillations on cavity drag, and a technique for their control. Ph.D. thesis, California Institute of Technology, Pasadena, California.

GOTTLIEB, D. O. & ORSZAG, S. A. 1977 *Numerical Analysis of Spectral Methods: Theory and Application.* SIAM.

GREINER, M. 1985 Experimental investigation of flow and transport enhancement in grooved channels. Ph.D. thesis, Massachusetts Institute of Technology, Cambridge, Massachusetts.

HERBERT, T. 1976 Finite amplitude stability of plane parallel flows. In *Proc. 5th Intl Conf. on Numerical Methods in Fluid Dynamics* (ed. A. I. Van de Vooren & P. J. Zandbergen). Lecture Notes in Physics, vol. 59, p. 235. Springer.

KARACHMETI, K. 1956 Sound radiated from surface cutouts in high-speed flows. Ph.D. thesis, California Institute of Technology, Pasadena, California.

KARNIADAKIS, G. E., BULLISTER, E. T. & PATERA, A. T. 1985 A spectral element method for solution of the two- and three-dimensional time-dependent incompressible Navier–Stokes equations. In *Proc. Intl Symposium on Finite Element Methods for Nonlinear Problems, Trondheim, Norway,* to appear.

KORCZAK, K. Z. & PATERA, A. T. 1985 An isoparametric spectral element method for solution of the Navier–Stokes equations in complex geometry. *J. Comp. Phys.* (to appear).

LANDAU, L. D. & LIFSHITZ, E. M. 1959 *Fluid Mechanics.* Pergamon.

MARCUS, P. S. 1984 Simulation of Taylor–Couette flow. Part 1. Numerical methods and comparison with experiment. *J. Fluid Mech.* **146**, 45.

MICHALKE, A. 1964 On the inviscid instability of the hyperbolic-tangent velocity profile. *J. Fluid Mech.* **19**, 543.

MEHTA, U. B. & LAVAN, Z. 1969 Flow in a two-dimensional channel with a rectangular cavity. *Trans. ASME E: J. Appl. Mech.* December.

MOFFATT, H. K. 1964 Viscous and resistive eddies near a sharp corner *J. Fluid Mech.* **18**, 1.

OSSWALD, G. A., GHIA, K. N. & GHIA, U. 1983 Study of incompressible separated flow using an implicit time-dependent technique. In *Proc. AIAA Computational Fluid Dynamics Conference, Danvers, Massachusetts.*

ORSZAG, S. A. 1971 Accurate solution of the Orr–Sommerfeld stability equation. *J. Fluid Mech.* **50**, 689.

ORSZAG, S. A. & PATERA, A. T. 1983 Secondary instability of wall-bounded shear flows. *J. Fluid Mech.* **128**, 347.

PAN, F. & ACRIVOS, A. 1967 Steady flows in rectangular cavities. *J. Fluid Mech.* **28**, 643.

PATERA, A. T. 1984 A spectral element method for fluid dynamics; laminar flow in a channel expansion. *J. Comp. Phys.* **54**, 468.

PATERA, A. T. 1985 Fast direct Poisson solvers for high-order finite element discretizations in rectangularly-decomposable domains. Submitted to *J. Comp. Phys.*

PRZMIENIECKI, J. S. 1963 Matrix structural analysis of sub-structures. *AIAA J.* **1**, 138.

REIHMAN, T. C. 1967 Laminar flow over transverse rectangular cavities. Ph.D. thesis, California Institute of Technology, Pasadena, California

ROCKWELL, D. 1982 Oscillations of impinging shear layers. *AIAA Paper No.* 82–0047.

ROCKWELL, D. & NAUDASCHER, E. 1979 Self-sustained oscillations of impinging free shear layers. *Ann. Rev. Fluid Mech.* **11**, 67.

SAROHIA, V. 1977 Experimental investigation of oscillations in flows over shallow cavities. *AIAA J.* **15**, 984.

STRANG, G. & FIX, G. J. 1973 *An Analysis of the Finite Element Method.* Prentice-Hall.